Synthesis of Tungsten-Modified Sn$_3$O$_4$ through the Cetyltrimethylammonium Bromide-Assisted Solvothermal Method for Dye Decolorization under Visible Light Irradiation

Mai Furukawa [1],*, Daichi Iwamoto [1], Koki Inamori [1], Ikki Tateishi [2], Hideyuki Katsumata [1],* and Satoshi Kaneco [1,2]

[1] Department of Applied Chemistry, Graduate School of Engineering, Mie University, Tsu 514-8507, Japan; 420m310@m.mie-u.ac.jp (D.I.); 423m308@m.mie-u.ac.jp (K.I.); kaneco@chem.mie-u.ac.jp (S.K.)

[2] Mie Global Environment Center for Education and Research, Mie University, Tsu 514-8507, Japan; tateishi@gecer.mie-u.ac.jp

* Correspondence: maif@chem.mie-u.ac.jp (M.F.); hidek@chem.mie-u.ac.jp (H.K.); Tel.: +81-59-231-9426 (M.F.)

Abstract: Novel tungsten-modified mixed-valence tin oxides (Sn$_3$O$_4$) with two oxidation numbers, such as Sn^{2+} and Sn^{4+}, were successfully prepared by the cetyltrimethylammonium bromide (CTAB)-assisted solvothermal method in one-step using tin (II) chloride dihydrate and sodium tungstate (IV) dihydrate as the precursors for dye degradation of methyl orange (MO) under visible light irradiation. The synthesized materials were characterized by various techniques to investigate the surface/structural morphology and the optical property. The presence of tungsten and the optimized amount of CTAB in the preparation method were favorable for the photocatalytic dye degradation reaction. In particular, when 0.03 of CTAB was added to W-modified Sn$_3$O$_4$ (W-Sn$_3$O$_4$@CTAB) and its concentration was 0.6 mg/mL, 10 mg/L of MO could be decolorized almost completely in 40 min, with the apparent reaction rate constant of 0.0496 min^{-1}. The improvement of photocatalytic activity for this proposed W-Sn$_3$O$_4$ results from increased reduction power, enhanced separation of electron–hole pairs, extended visible light absorption range, and optimized band structure by CTAB additive. The radical trapping experiments showed that the main reactive species during the photocatalytic reaction are superoxide ions. The developed photocatalysts may contribute to the development of environmental improvement technology.

Keywords: Sn$_3$O$_4$; cetyltrimethylammonium bromide; solvothermal method; decolorization; photocatalysis; visible light irradiation

1. Introduction

Water pollution caused by organic dyes is one of the serious problems with the development of the printing and dyeing industry [1]. Among the diverse source of water contaminants, azo dyes with one or more azo groups (-N=N-) as the chromophore and other functional groups commonly have toxicity, mutagenicity, and low degradability [2,3]. Such dye pollutants with sewage and/or industrial wastewater were discharged into the environment without being purified, resulting in serious pollution problems [4,5]. The dyes released into the environment remain for a long time, worsening water quality, reducing light penetration, and affecting the performance of aquatic organisms, and ultimately, they can have significant negative impacts on the life of aquatic organisms, humans, and other mammals through oral ingestion and/or skin contact [6,7]. Hence, there is an urgent need for novel technology development to treat dye-contaminated wastewater safely and efficiently.

While many water treatment technologies, including physical, chemical, and biological approaches have been implemented, photocatalysis has been recognized as one of the most important and green technologies to solve water pollution problems [8–11].

In particular, many strong and sustainable approaches have been conducted to design novel photocatalytic materials for the efficient decomposition of pollutants by the application of visible light, which accounts for the largest proportion of the solar spectra as a renewable energy [12,13].

Recently, there has been a significant interest in tin-based oxide materials in photocatalysis. Among them, tin dioxide (SnO_2) is an n-type semiconductor with a band gap of 3.7 eV with many advantages such as low cost, lack of toxicity, environment-friendly, and high photoelectrochemical performance [14,15]. In contrast, its wide band limits the photocatalytic activities under solar energy since SnO_2 materials can only absorb ultraviolet light, and the rapid recombination rate of the photogenerated electron–hole pair reduces its photocatalytic efficiency [16]. In order to overcome these disadvantages, the turning of morphology has attracted much attention in recent years, and attempts have been made to synthesize tin oxides with unique morphological structures [17]. Sn_3O_4, as a metal oxide with a mixed valence state of Sn^{2+} and Sn^{4+}, has been reported to have strong solar absorption and high chemical stability [18,19]. Although Sn_3O_4 has improved visible light responsivity like other photocatalysts, it has problems with the recombination rate of electrons and holes and the charge transfer rate [20]. Another effective approach to designing visible-light-driven photocatalysts is the modification of photocatalytic materials employing metals and/or nonmetals by doping impurity elements and other noble metal depositions [21,22]. It is reported that the introduction of high-valence cations such as tungsten for the photocatalysts modifies the electronic structure of its material [23,24]. In the combination of tin and tungsten, tin tungstate ($SnWO_4$), as one of metal tungstates, has gained attention for its unique structure and optical properties as a multi-metal oxide semiconductor [25,26]. On the other hand, to the best of our knowledge, few reports have developed photocatalysts consisting of tungsten modified with tin oxide, and the mechanisms of those photocatalysts under visible light irradiation remain far from clear.

In the preparation of functional materials, adjusting the final photocatalyst morphology is important to obtaining a large surface area and high photoactivity for high photocatalytic efficiency [27]. In order to control the morphology of the catalysts by manipulating the growth of particles, it is common to introduce a variety of organic additive agents such as polyvinylpyrrolidone (PVP) [28], polyethylene glycol (PEG) [29], and ethylenediaminetetraacetic acid (EDTA) [30,31]. Among them, cationic surfactants such as cetyltrimethylammonium bromide (CTAB) are widely used to regulate crystal growth, surface structure, and optical properties as a structure-directing agent [32]. Currently, the influence of CTAB as a capping agent on the photocatalytic activity of Sn_3O_4 has been seldom addressed.

In this work, visible-light-driven tin oxide-based photocatalysts were synthesized using the CTAB-assisted solvothermal method with tungsten as another metal. The influence of the presence of tungsten and CTAB quantity on the photocatalytic efficiency of these photocatalysts was evaluated through the dye degradation rate of methyl orange under visible light irradiation. The crystal structure, morphology observation, and chemical properties of the photocatalysts were used to examine the reaction mechanism via various techniques. Consequently, we present the first successful introduction of tungsten into Sn_3O_4 with effective CTAB support, achieving a visible-light-driven photocatalyst to promote dye decolorization.

2. Results and Discussion

2.1. Crystallographic Phase Properties

Figure 1a,b shows the prepared photocatalysts' X-ray diffraction (XRD) patterns. It can be seen that the diffraction patterns of all synthesized samples are attributed to triclinic Sn_3O_4 according to the standard card (JCPDS NO.16-0737), along with corresponding reflections of the (111), (210), (122), (130), (132), and (013) lattice planes at 26.4°, 32.9°, 34.0°, 38.6°, 51.8°, and 61.9° as 2θ values, respectively [33,34]. For W-modified Sn_3O_4 samples, no obvious peaks related to tungsten species were detected, which might be due to the lower

content of W. The diffraction peaks of W-Sn$_3$O$_4$ samples slightly shift towards the lower angle side as compared with unmodified tungsten Sn$_3$O$_4$, which indicates lattice expansion with W-modification because of the large crystal radius of tungsten [35]. At the same time, it was expected that the decrease in crystallinity and the broadening of the diffraction peak occurred via changes in the crystal structure due to the presence of tungsten in tin oxides. Moreover, in comparison to the XRD pattern of sodium tungstate (IV) dihydrate shown in Figure 1c, no specific peaks of tungsten precursor were identified in the prepared samples, suggesting that tungsten, in elemental form, is introduced into Sn$_3$O$_4$ materials. Compared to Sn$_3$O$_4$ samples prepared with and without CTBA (0.03 g), almost no change in these XRD patterns was observed, and no characteristics for any other phases about impurities could be detected. The results indicate that the CTAB in the solvent for the solvothermal method has no significant effect on the crystal structure of the catalyst.
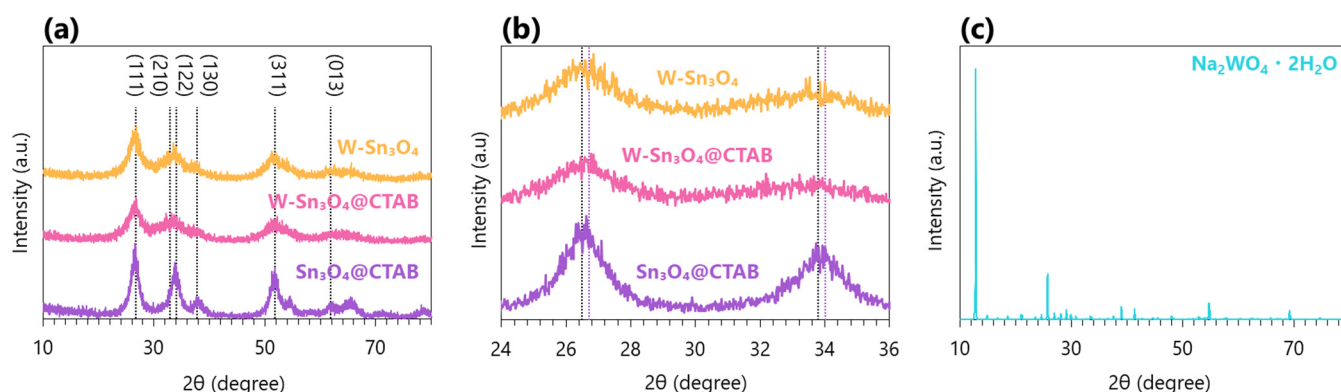

Figure 1. (**a**) XRD patterns, (**b**) the enlarged spectra in the range of 24 to 36 degrees of Sn$_3$O$_4$@CTAB, W-Sn$_3$O$_4$@CTBA, and W-Sn$_3$O$_4$, and (**c**) XRD pattern of pure sodium tungstate (IV) dihydrate as 2θ values.

2.2. Surface Morphology

The scanning electron microscopy (SEM) images in Figure 2a–c indicated that all prepared samples exhibited lump-shaped structures. It was observed that the addition of tungsten to tin oxides resulted in finer surface morphology, and the appropriate amount of CTAB in the photocatalysts preparation led to the formation of an even finer microstructure. On the other hand, it also demonstrated that the shape of the products could not be radically altered by two factors, within the scope of an investigation, in the proposed preparation method. In Figure 2d,e, the transmission electron microscopy (TEM) images show that each synthesized sample contains irregular aggregations of various sizes as indicated by the SEM observations. In the case of W-Sn$_3$O$_4$ without CTAB, many crystals around 30 nm were found, and the aggregation degree of these crystals was high; by contrast, smaller crystals of around 10 nm were observed for the W-Sn$_3$O$_4$@CTAB. Moreover, Sn$_3$O$_4$@CTAB was constituted by aggregates of smaller crystals than W-Sn$_3$O$_4$@CTAB. The modification of the crystalline shape by tungsten and CTAB might be beneficial to facilitate photocatalytic performance by providing the reaction active sites.

For additional photocatalytic surface characterization studies, specific surface areas related to physical adsorption and photocatalytic activity were obtained via the BET method using nitrogen. As shown in Figure 3a, it was reported from the nitrogen adsorption/desorption isotherm analysis that the curve shapes of all products belonged to type-IV isotherms with H3-type hysteresis loops characteristic of the mesoporous structure. The corresponding pore sizes distribution curves in Figure 3b, also analyzed from the desorption branch of the isotherms, were calculated via Barret Joyner Halenda (BJH) methods [36]. It can be seen that the diameter range of pores was found to be concentrated between 2 and 20 nm for all photocatalysts measured, which further confirmed the mesoporous character of their materials. Table 1 shows that BET-specific surface area tended to increase

with W modification and stabilize around 40 cm^3/g as a result of the decrease in surface area with the addition of CTAB; however, this appeared to have little correlation with photocatalytic activity.
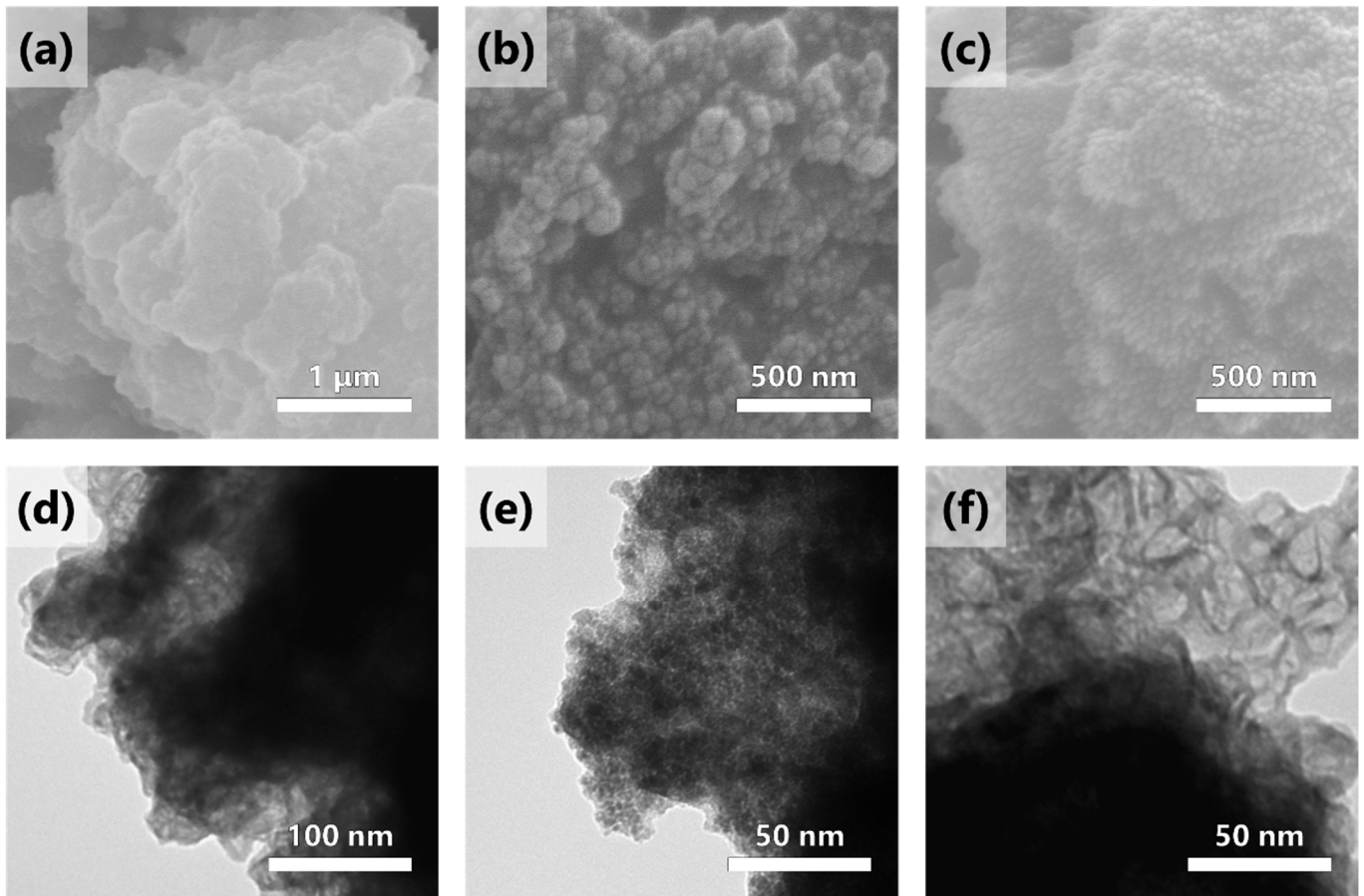
Figure 2. SEM and TEM images of (**a**,**d**) W-Sn$_3$O$_4$, (**b**,**e**) Sn$_3$O$_4$@CTAB, and (**c**,**f**) W-Sn$_3$O$_4$@CTAB.
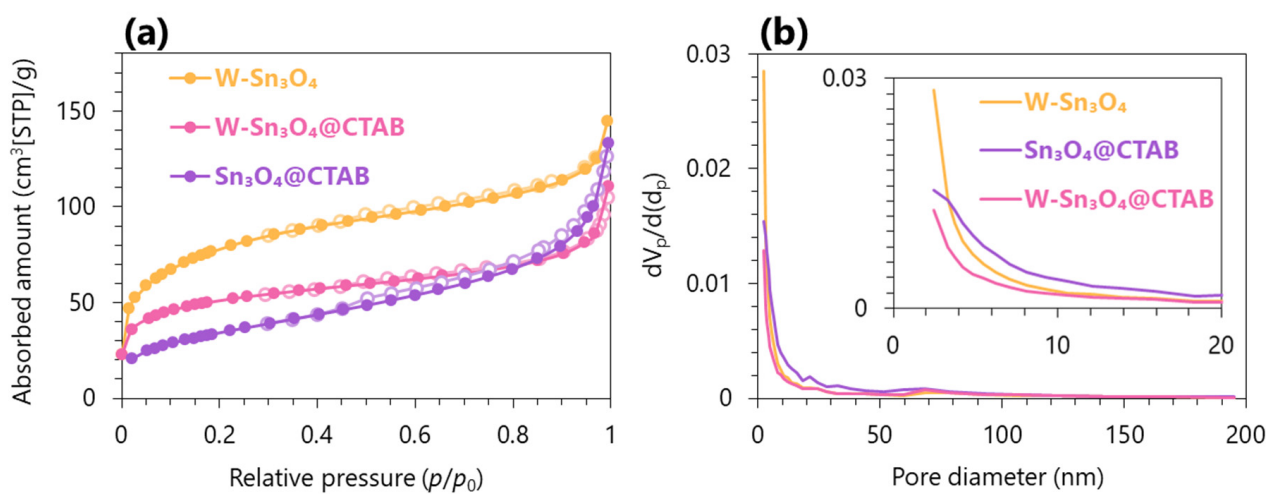

Figure 3. (**a**) Nitrogen adsorption/desorption isotherms and (**b**) the corresponding pore size distribution curves of the synthesized samples.

Table 1. Monomolecular layer adsorption volume (V_m), BET specific surface area (a_{sBET}), total pore volume (V_p), and average pore diameter (d_p) of the synthesized samples.

Sample	CTAB Amount	V_m (cm³(STP)/g)	a_{sBET} (m²/g)	V_p (p/p₀ = 0.990)(cm³/g)	d_p (nm)
Sn_3O_4	0.03 g	28.5	124.0	0.20	6.36
$W-Sn_3O_4$	0.03 g	42.8	186.0	0.17	3.54
$W-Sn_3O_4$	0 g	64.6	281.4	0.22	3.14

Therefore, the improvement of photocatalytic activity for dye degradation of MO would largely be attributed to various modified optical properties rather than to the optimization of the surface morphology.

2.3. Chemical Structure

The chemical structural information about the chemical bonding or molecular structures of materials can be illustrated via Fourier-transformed infrared (FT-IR) spectra in Figure 4a. The characteristic peaks at 2918 cm⁻¹ and 2850 cm⁻¹ correspond to the C–H bond stretching vibration from methyl and methylene groups of CTAB. Because the two absorption bands mentioned above were observed around 2900 cm⁻¹ in the materials prepared with CTAB (Sn_3O_4@CTAB and $W-Sn_3O_4$@CTAB), a small number of linear molecules of CTAB are present inside or on the surface [37]. Other peaks observed in CTAB were attributed to the alkyl chains as hydrophobic groups. The strong and wide band around 3400 cm⁻¹ arises from the stretching vibration of hydroxyl groups on surface hydroxyl groups or adsorbed water due to the re-adsorption of water from the ambient atmosphere. The broad band around 500 cm⁻¹ and 1470 cm⁻¹ is caused by the vibration of the Sn–O bond and the bending vibration of Sn-OH, respectively [38]. Due to the trace amount of modified tungsten, there was no evidence of its presence in the W–O bond.
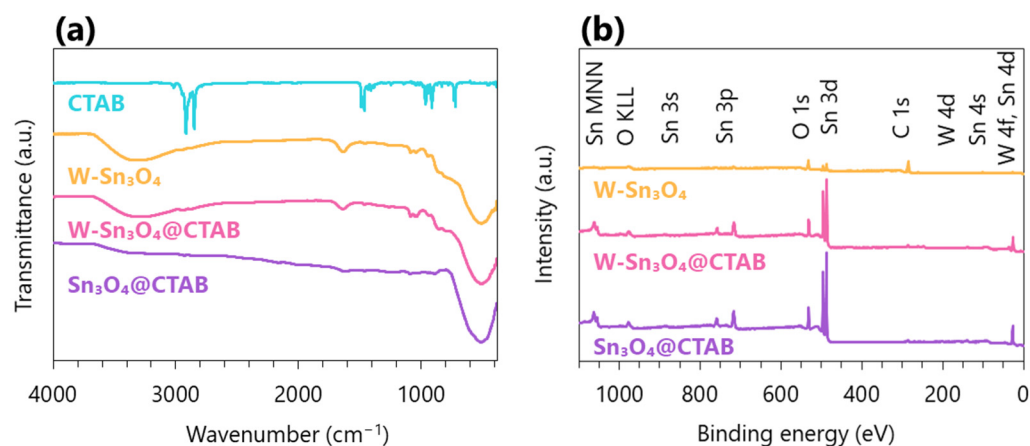
Figure 4. (**a**) FT-IR and (**b**) XPS survey spectra of the synthesized samples.

The further chemical surface compositions and elemental valence states of the prepared samples were identified via X-ray photoelectron spectroscopy (XPS) analysis. The survey XPS spectra in Figure 4b of all samples finds the peaks originating from C, O, and Sn elements. In addition, the peaks related to the W element are also detected in the samples treated with tin and tungsten precursors simultaneously via the solvothermal method, indicating that the tungsten was assuredly doped in Sn_3O_4-based photocatalysts. In contrast, the peaks of nitrogen (N) and bromine (Br), which could be derived from CTAB employed in the sample preparation process, were not observed even via high-resolution spectral analysis. This result is consistent with the result from the XRD and FT-IR techniques.

The C 1s spectra in Figure 5a show three binding energy peaks at 284.8 eV, 286.2 eV, and 288.7 eV associated with C single bond C (C–C), C single bond O (C–O), and O

single bond C single bond O (O–C–O) groups, respectively. These peaks indicate that the synthesized samples contain some carbon originating from the background carbon as well as hydrocarbons, including CTAB.
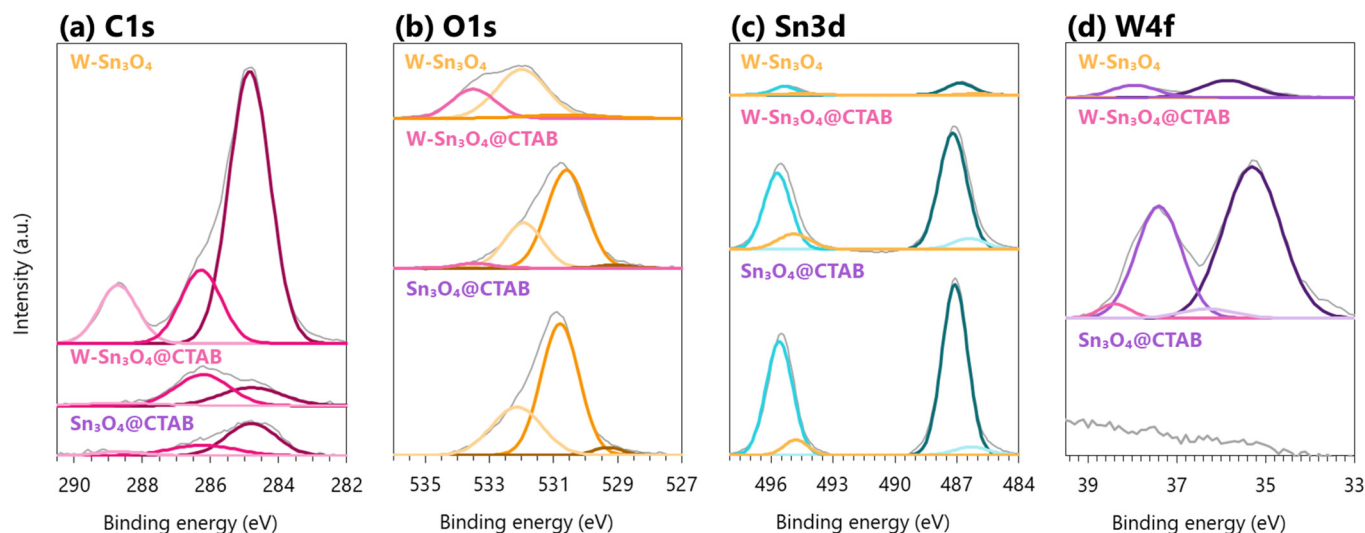

Figure 5. XPS high-resolution spectra of (**a**) C1s, (**b**) O1s, (**c**) Sn3d, and (**d**) W4f showing Sn_3O_4@CTAB in the bottom, W-Sn_3O_4@CTAB in the middle, and W-Sn_3O_4 in the top.

The O1s spectra in Figure 5b show the apparent peak around 530 eV attributed to crystal lattice oxygens. In particular, each binding energy of Sn_3O_4@CTAB, W-Sn_3O_4@CTAB, and W-Sn_3O_4 are located at 530.8 eV, 530.6 eV, and 530.6 eV, respectively, where there appear to be slight shifts of about 0.2~0.3 eV to lower binding energy due to the adjustment of the metals–oxygen bonding state via W-modification and CTAB additive. Other small shoulders are observed at 530.0 eV and 533.5 eV, probably due to adsorbed water molecules on the surface and the hydroxyl groups, respectively.

Sn 3d XPS spectra of Sn_3O_4-based samples in Figure 5c display two splitting peaks consisting of Sn 3d3/2 and Sn 3d5/2 states, which are further separated into the peaks belonging to Sn^{2+} and Sn^{4+}. Moreover, the asymmetric shape of Sn 3d XPS spectra is attributed to the fact that Sn has different chemical states within the Sn_3O_4 crystal lattice. With respect to Sn_3O_4 photocatalysts-modified W, four fitted subpeaks at 486.4 eV, 487.2 eV, 494.9 eV, and 495.7 eV were ascribed to $3d_{5/2}$ Sn^{2+}, $3d_{5/2}$ Sn^{4+}, $3d_{3/2}$ Sn^{2+}, and $3d_{3/2}$ Sn^{4+}, respectively, and the binding energy of Sn 3d slightly shifts toward the high energy direction compared to the Sn_3O_4 sample without tungsten.

No characteristic peaks of the tungsten element are detected in pure Sn_3O_4@CTAB in Figure 5d. The main oxidation state of tungsten detected on the W-Sn_3O_4 photocatalysts is a valency of six, having peaks at around 35.9 eV and 38.0 eV for $W4f_{7/2}$ and $W4f_{5/2}$, respectively. As CTAB concentration increased, two W4f peaks shifted toward the lower binding energy side. The change of binding energy may be related to the change of electron density in the materials. The results of each peak shift for Sn 3d, and W 4f support the successful modification of tungsten to Sn_3O_4-based samples. Furthermore, a trace amount of pentavalent tungsten (W^{5+}) was detected during W 4f peak resolution stage. In previous works, it has been reported that group-6 W works as a singly charged donor (W^{5+}) in tetravalent cation-based SnO_2 because the ionic radius of tungsten was close to that of tin [39,40]. Therefore, the same phenomenon is expected to have occurred in these proposed photocatalysts.

Even though the amount of tin and tungsten used during the solvothermal process were the same, the peak intensity of O, Sn, and W as the main constituents of the samples with CTAB were provably stronger than those without CTAB; CTAB worked well as a structure-directing agent to adjust the final photocatalyst morphology.

2.4. Optical Property

In photocatalytic reactions, the recombination of photoinduced electron–hole pairs significantly affects their activity [41]. Therefore, photoluminescence (PL) measurements were performed to investigate the efficiency of free charge carriers trapping and transfer in the proposed photocatalysts via the intensity of fluorescence produced when photoinduced electrons recombine with holes, as shown in Figure 6a. The synthesized samples showed a visible emission centered around 420 nm. The PL intensity of W-Sn_3O_4 is lower than that of Sn_3O_4 without tungsten in the same wavelength range, which was attributed to interference with the recombination of photoinduced electrons and holes because the tungsten could act as an electron trapping site. The fluorescence emission of W-Sn_3O_4 with the proper quantity of CTAB was further significantly inhibited, suggesting the presence of possible defects and/or the optimized band structure in the photocatalysts induced by the structure-directing agent.
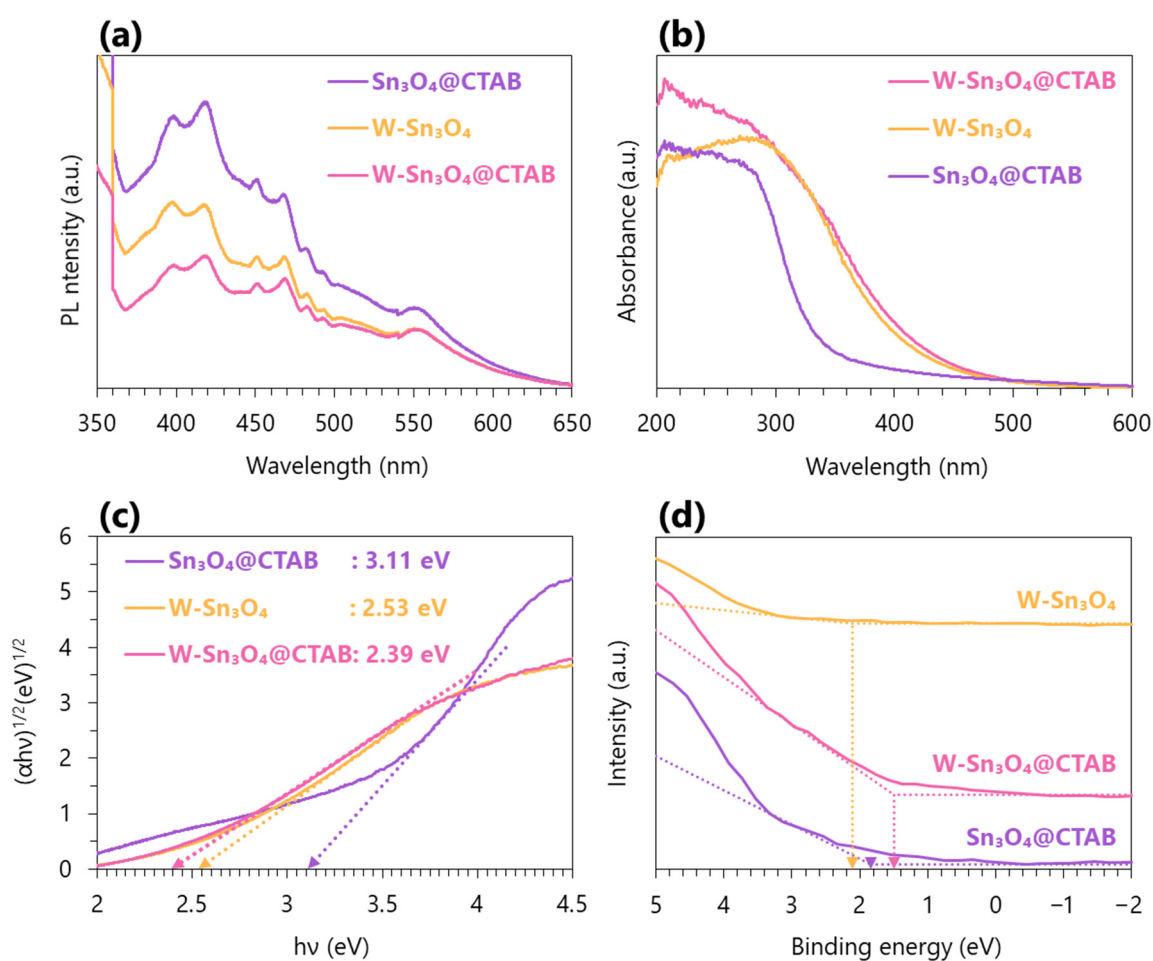

Figure 6. (**a**) PL, (**b**) DRS, (**c**) Tauc-plots of the optical indirect band gap of the photocatalysts with dotted lines as tangents to determine the bandgap energies, and (**d**) VBXPS with dotted lines as tangents to determine the valence band positions for each photocatalysts.

The optical property of the prepared photocatalysts was investigated via UV–vis diffuse reflectance spectra (DRS) in Figure 6b. Here, the optical band gap of a crystalline semiconductor follows the equation:

$$\alpha h\nu = A(h\nu - E_g)1/n, \tag{1}$$

where α, $h\nu$, E_g, and A are absorption coefficient, incident photon energy, band gap energy, and a constant, respectively. Among them, n depends on the type of optical transition of

a semiconductor ($n = 1/2$ for direct transition and $n = 2$ for indirect transition) [42]. The band-to-band excitations of Sn_3O_4-based photocatalysts in this work exhibited indirect transitions [43,44]. The intercept of the tangent to the *x*-axis gives the approximation of the bandgap energy.

Although the Sn_3O_4 without W sample could almost absorb only UV light due to the large band gap energy (3.11 eV), the optical absorption range of the W-modified Sn_3O_4 samples is significantly extended to the visible light region. In addition, compared to those of W-Sn_3O_4 prepared with and without CTAB, the absorption edge of CTAB-assisted W-Sn_3O_4 was red-shifted to longer wavelengths in the visible region. The optical band gap energy was found to be 3.11, 2.39, and 2.53 eV for Sn_3O_4@CTAB, W-Sn_3O_4@CTAB, and W-Sn_3O_4, respectively. Therefore, the results indicated that W-modification and CTAB-assist procedure for Sn_3O_4 preparation effectively adjust the band gap energy (E_g) of photocatalysts for dye degradation under visible light irradiation.

The valence band (VB) positions of the prepared photocatalysts were determined via VBXPS analysis. After reading the VBXPS values from Figure 6d, the contact potential difference between the samples and the analyzer was corrected based on the following equation:

$$E_{NHE} \text{ (V)} = VBXPS - 4.44 + \varphi, \tag{2}$$

where E_{NHE} and φ are the standard electrode potential and electron work function of the analyzer (4.33 eV in this work), respectively [45]. As a result, the VB positions of Sn_3O_4@CTAB, W-Sn_3O_4@CTAB, and W-Sn_3O_4 were estimated to be 1.73 V, 1.31 V, and 2.00 V, respectively.

From the band structure of each catalyst obtained by the combination of VBXPS and DRS results, it was revealed that the energy band, regulated to a bandgap to be responsive in visible light via the tungsten introduction, was placed on the lower potential side by the CTAB additive.

2.5. Electrochemical Characterization

The separation efficiency of the photogenerated electron–hole pairs in the photocatalyst was analyzed using a three-electrode system. As seen from the electrochemical impedance spectroscopy (EIS) Nyquist plots in Figure 7a, the W-Sn_3O_4@CTAB photocatalyst exhibits the smallest arc radius with a lower charge transfer resistance, which means that the sample exhibited the highest electron transport rate. Transient photocurrent response (I-t) analysis of the prepared samples was then performed to verify numerous on–off cycles under visible light. The W-Sn_3O_4@CTAB photocatalyst showed a good photocurrent response, suggesting that the structure modified by tungsten and CTAB with great synergistic interactions can effectively transfer the excited charge carriers and shorten the reunion rate.
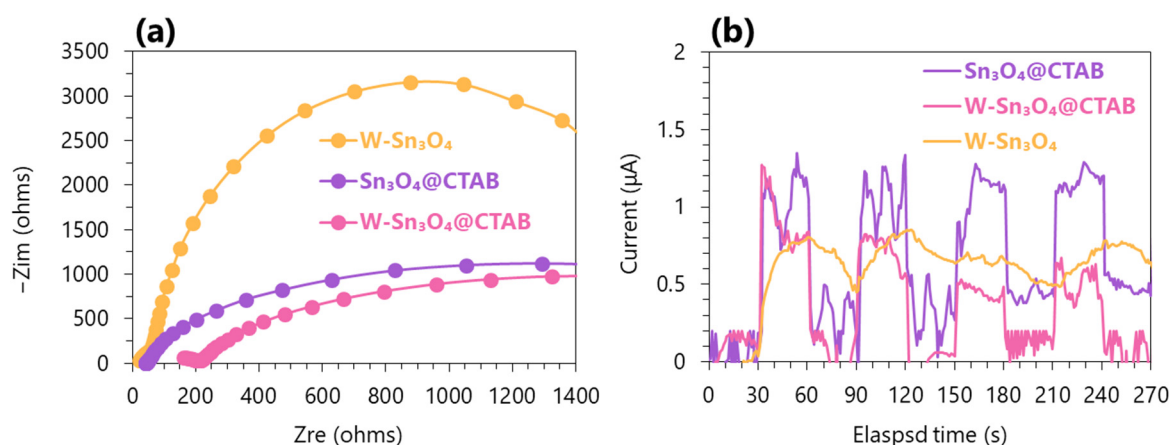

Figure 7. (**a**) Nyquist plots and (**b**) the transient photocurrent response.

2.6. Photocatalytic Dye Degradation

The photocatalytic activity of Sn_3O_4-based photocatalysts prepared under various conditions, such as tungsten modification and CTAB amount in the solvothermal method, were evaluated via the photodegradation of MO under visible light irradiation ($\lambda \geq 420$ nm). In order to acquire the MO degradation efficiency, the degradation rate C/C_0 and the apparent rate constant k (min^{-1}) of the photocatalysts were calculated. Here, the experimental data corresponded to the first-order Langmuir–Hinshelwood (L–H) model owing to the low MO concentration, and pseudo-first-order kinetics could be obtained via the following formula:

$$-\ln(C_0/C_t) = kt, \tag{3}$$

where C_0 and C_t represent the initial concentration after adsorption/desorption equilibrium and the concentration at light irradiated time t (min) during the photoreaction.

Figure 8a shows the photocatalytic activity of Sn_3O_4 and W-Sn_3O_4, each containing 0.03 g of CTAB. Sn_3O_4 modified without tungsten had no ability to decolorize MO under visible light irradiation, which is attributed to its narrow absorption wavelength region and wide band gap as shown in the DRS results. In contrast, W-Sn_3O_4 is visible-light-driven, which explains that the optimized structure by tungsten species incorporated in Sn_3O_4 provides more reaction active sites and facilitates the efficient transfer and separation of charge carriers. Figure 8b shows the photocatalytic activity of W-Sn_3O_4 with different CTAB amounts (0~0.2 g). The photocatalytic degradation efficiency of MO improved with an increasing CTAB amount in the solvothermal method, and W-Sn_3O_4 containing 0.03 g of CTAB, with the highest photocatalytic decolorization performance, could decolorize 99% of MO within 40 min. The reaction rates of the W-Sn_3O_4 with 0, 0.01, 0.02, 0.03, 0.04, 0.05, and 0.2 g of CTAB additive were 0.0091, 0.0361, 0.0445, 0.0404, 0.0203, and 0.0181 min^{-1}, respectively. In short, W-Sn_3O_4@CTAB (0.03 g) obtained the maximum rate constant, which is about 5.5 times faster than that of pure W-Sn_3O_4. On the other hand, the excess quantity of CTAB resulted in photocatalytic reaction inhibition. From the characterization results, that the optimized amount of CTAB (0.03 g) can significantly enhance the photocatalytic performance of W-Sn_3O_4, originating from the effective separation of photo-induced carriers and DRS redshift, is distinct. Based on the above results, two approaches for Sn_3O_4, tungsten induction as well as CTAB addition, were found to be superior for photocatalytic MO decolorization under visible light irradiation.

The pH of the sample solution is one of the essential factors that can directly influence the diffusion process, surface adsorption, and surface charge of dyes. The effect of the sample solution pH on photocatalytic decolorization of MO in the presence of W-Sn_3O_4@CTAB (0.03 g) was investigated in the range of pH 3–9. As shown in Figure 8c, the photocatalyst exhibited high decolorization efficiency under acidic conditions; however, the photocatalytic activity decreased as pH values increased. The decolorization efficiencies at 60 min of light irradiation were 99, 99, 62, and 40%, and the reaction rate constants were 0.0700, 0.0496, 0.0213, and 0.0106 min^{-1} at pH values of 3, 5, 7, and 9, respectively. It has been reported that Sn_3O_4-based materials exhibit the isoelectric point on the acidic side [46]; therefore, the W-Sn_3O_4@CTAB surface is likely to be protonated around pH 3 and/or 5. Combined with the knowledge that methyl orange is an anionic dye, the difference in catalytic activity at each solution pH appears to be interactions such as electrostatic attraction/repulsion between the catalyst and MO. In addition, the competition between hydroxide ions and negatively charged MO in basic solutions could contribute to reduced photocatalytic activities under high pH conditions.

The comparison of the performance of W-Sn_3O_4@CTAB as the prepared photocatalyst with other photocatalytic techniques in several references is shown in Table 2 [47–51]. The proposed photocatalyst preparation technique based on a one-step solvothermal method is facile, and the photocatalytic activities for MO decolorization reported in this study is good or comparable to that of other photocatalysts reported in other literature and possibly related to W-Sn_3O_4@CTAB.
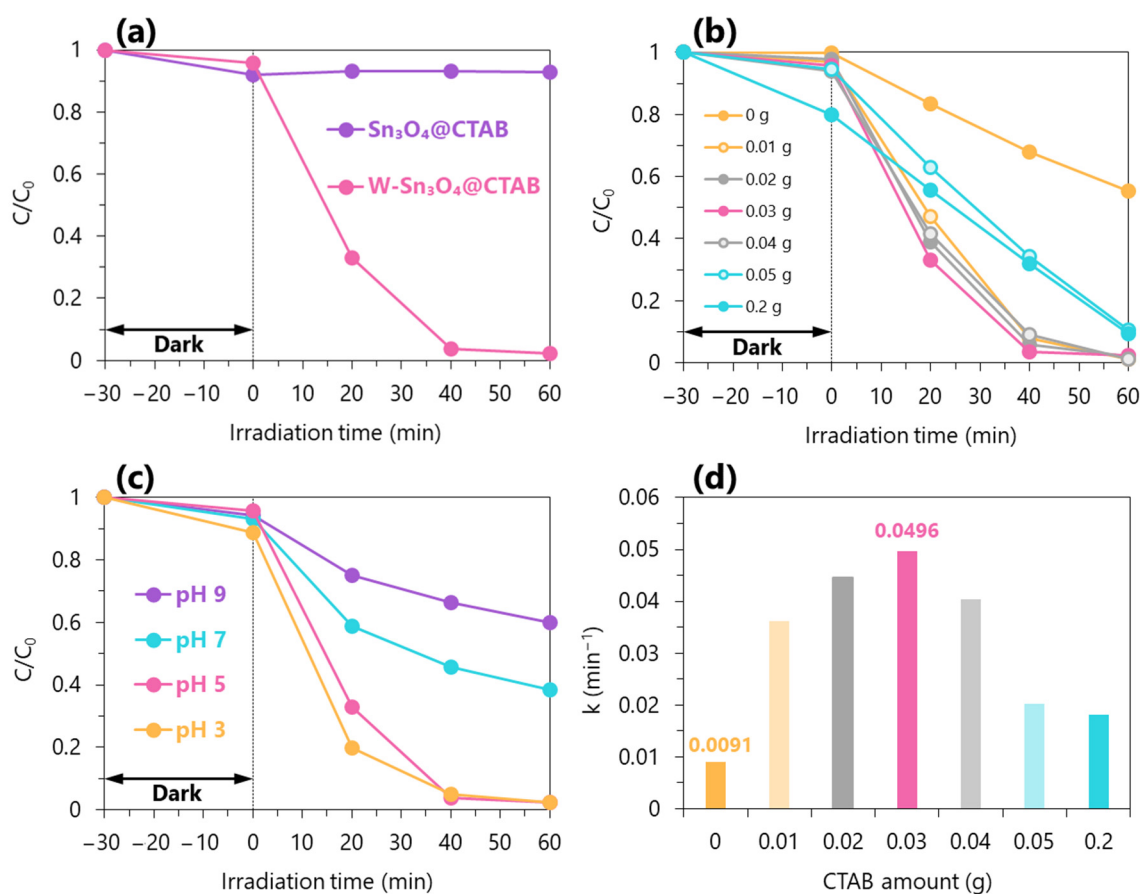
Figure 8. Effect of (**a**) tungsten modification, (**b**) amount of CTAB in the proposed preparation method, and (**c**) pH of the sample solution in the dispersion of W-Sn_3O_4@CTAB (0.03 g) on photocatalytic decolorization of MO under visible light irradiation, and (**d**) the apparent reaction rate constant of each photocatalyst with different amounts of CTAB.

Table 2. Comparison of photocatalytic performance of the prepared W-Sn_3O_4@CTAB and a few other photocatalysts for methyl orange decolorization.

Photocatalyst	Preparation Method	Light Source	Photocatalyst Concentration (mg/mL)	MO Concentration (mg/L)	Efficiency (%)	Time (min)	Ref.
WO_3/g-C_3N_4	Thermal polymerization	300 W xenon lamp	1	10	93	120	[47]
TiO_2@ WO_3	Etching + hydrolysis processes	300 W xenon lamp	1	10	95	25	[48]
N-CQDs/Sn_3O_4	CQDs process + hydrothermal	500 W xenon lamp	0.6	10	78	80	[49]
Ni-Sn_3O_4	One step hydrothermal	300 W xenon lamp	1	10	72	60	[50]
S-Sn_3O_4	One step hydrothermal	500 W xenon lamp	1	20	99	80	[51]
W-Sn_3O_4@CTAB	One step solvothermal	500 W xenon lamp	0.6	10	99	40	This work

2.7. Reaction Mechanisms

Investigation of the intermediates involved in photocatalytic reactions is important to revealing the mechanisms. The radical trapping experiments were performed to determine the reactive species of W-Sn_3O_4@CTAB (0.03 g) in the photocatalytic process. In the present work, we attempted to trap superoxide radical anions ($\bullet O_2^-$), hydroxyl radicals ($\bullet OH$), and photogenerated holes (h^+) that are critical in the oxidation reaction by adding scavengers

such as benzoquinone (BQ), isopropyl alcohol (IPA), and ethylene diamine tetraacetic acid (EDTA). As shown in Figure 9, the degradation efficiency significantly decreased in the presence of BQ (-100%) and slightly decreased in the presence of IPA (-67.6%) and EDTA (-17.6%) compared with the blank experiment. Hence, it is concluded that superoxide radical anions are the main reactive component in the MO decolorization in the presence of visible light irradiation catalyzed by W-Sn_3O_4@CTAB.
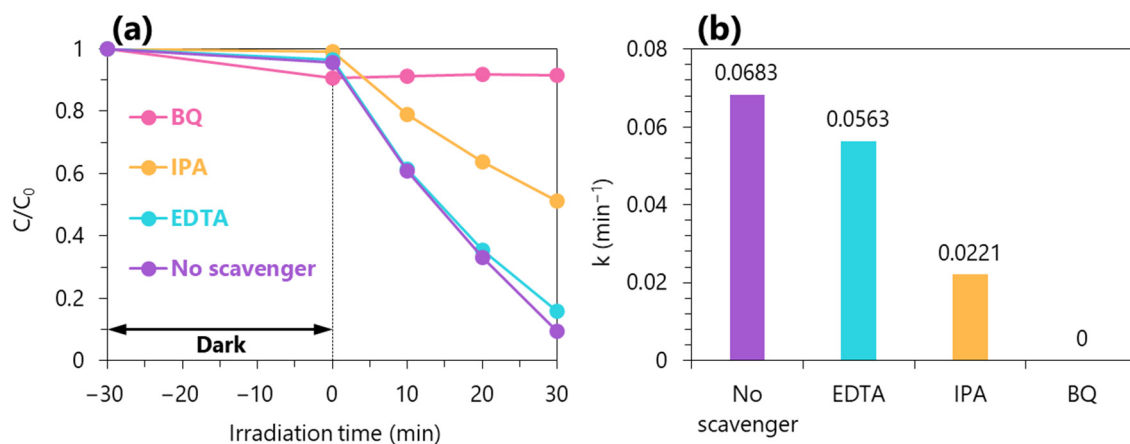

Figure 9. Free radical trapping experiment from (**a**) MO decolorization efficiency and (**b**) apparent reaction rate constant over W-Sn_3O_4@CTAB.

In summary of the above results, the suggested photocatalytic mechanism and photoinduced charge transfer during MO decolorization on the proposed photocatalysts are shown in Figure 10. First of all, due to the introduction of tungsten into mixed-valence tin oxides (Sn_3O_4), the visible-light-harvesting performance of W-Sn_3O_4 materials was considerably enhanced. In detail, new impurity levels originating from tungsten owing to its multiple oxidation states are formed within the broadband structure with limited photoresponsivity of Sn_3O_4, resulting in decreased bandgap energy. Moreover, the addition of CTAB during crystal growth further optimizes the final photocatalytic morphology, with this result leading to improved visible-light absorption ability.
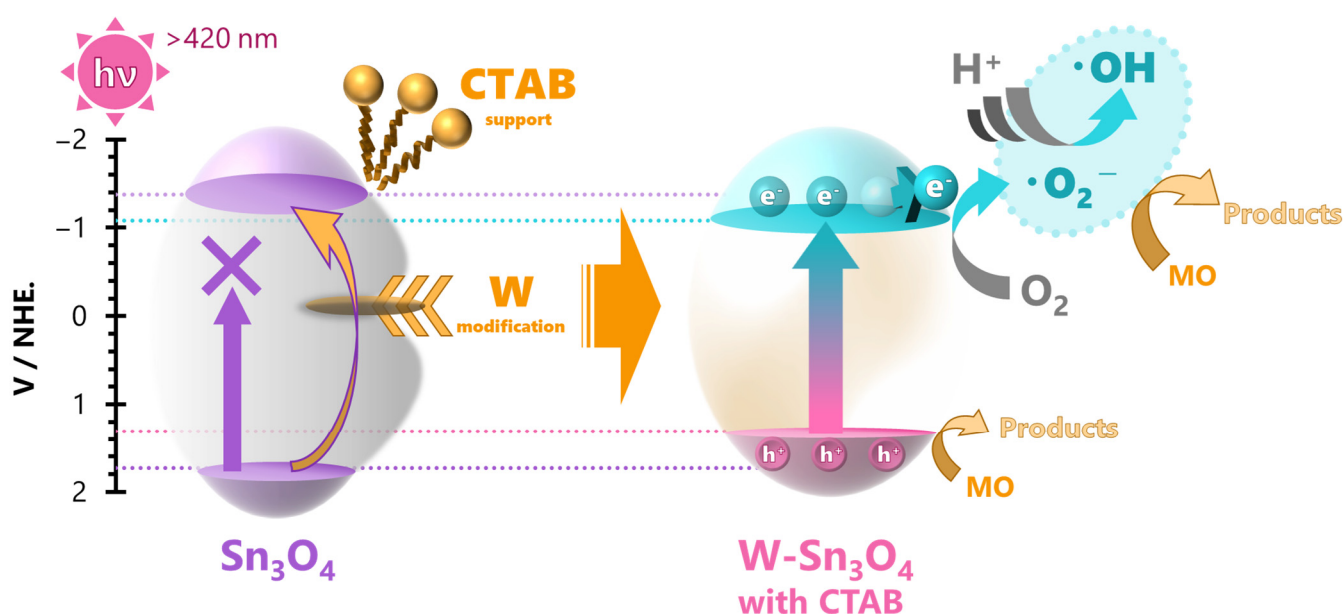

Figure 10. Photocatalytic mechanism of W-Sn_3O_4@CTAB under visible light irradiation.

During the photocatalytic process under visible light irradiation, the electrons (e^-) from the valence band (VB) are forced to move into the conduction band (CB) with the generation of the same number of holes (h^+). Although the photogenerated electrons and holes generally recombine rapidly, those active species immediately move to the catalyst surface because the designed W-Sn_3O_4@CTAB photocatalyst possesses excellent electron transfer and collection ability. The redox potentials of $O_2/\bullet O_2^-$ have been reported to be equal to -0.33 V [52]; thus, the photoexcited electrons can be transferred to the adsorbed oxygen on the surface of W-Sn_3O_4 to form the superoxide radical anions ($\bullet O_2^-$), whereas hydroxyl radicals have a very high potential for oxidation (2.80 V) [53], which means that the holes in the VB around 1.31 eV cannot interact with OH- and/or H_2O adsorbed on the photocatalyst surface to produce $\bullet$OH. Therefore, the superoxide radical anions would receive hydrogen ions to form protonated superoxide anion radicals (HOO$\bullet$); then, HOO$\bullet$ would receive a hydrogen ion to form H_2O_2 and be converted to $\bullet$OH [54]. The produced reaction active species are eventually involved in the oxidation reaction of MO. In addition, the photoproduced holes not consumed for $\bullet$OH formations could also oxidize MO directly.

3. Materials and Methods

3.1. Materials

All of the chemicals were of analytical grade and used without further purification. Tin (II) chloride dihydrate ($SnCl_2 \cdot 2H_2O$) was purchased from NACALAI TESQUE, INC., Japan. Sodium tungstate (IV) dihydrate ($Na_2WO_4 \cdot 2H_2O$), cetyltrimethylammonium bromide (CTAB, $C_{19}H_{42}BrN$), ethylene glycol ($C_2H_6O_2$), sodium hydroxide (NaOH), and methyl orange ($C_{14}H_{14}N_3NaO_3S$) were obtained from FUJIFILM Wako Pure Chemical Co., Osaka, Japan. The distilled water prepared by the water distillation apparatus RFD260NC was used throughout all experiments.

3.2. Preparation of Photocatalysts

W-modified Sn_3O_4 (W-Sn_3O_4) photocatalysts were prepared via a one-pot solvothermal method. Typically, 1 mmol tin (II) chloride dihydrate was dissolved in 30 mL ethylene glycol and mechanically stirred. In another vessel, sodium tungstate (IV) dihydrate was dissolved in 20 mL ethylene glycol by ultrasonic treatment, and then CTAB was added to the mixture to form Na_2WO_4-CTAB solution. Na_2WO_4-CTAB solution was added slowly dropwise to $SnCl_2$ solution under stirring thoroughly. The pH value of its solution was adjusted with 10 mol/L NaOH aqueous solution. The resulting suspension was continuously stirred for 1 h and then treated via a solvothermal process in a 100 mL Teflon-lined autoclave at 200 °C for 18 h. After the system was naturally cooled to ambient temperature, the precipitate was centrifuged, washed with distilled water and ethanol several times, and dried at 60 °C for 6 h in a vacuum oven to obtain the main body of the photocatalysts. Additionally, Sn_3O_4 with CTAB and W-Sn_3O_4 without CTAB were prepared by using the procedures mentioned above in the absence of Na_2WO_4 and CTAB, respectively.

3.3. Characterization

X-ray diffraction (XRD) patterns were recorded by a RIGAKU Ultima IV instrument with a Cu-Kα radiation source for structural analysis. X-ray photoelectron spectroscopy (XPS) spectra were employed to investigate chemical bonding states. All binding energies of photocatalysts were calibrated with C1s peak of the surface adventitious carbon at 284.8 eV as the reference. Fourier transform infrared (FT-IR) spectra were obtained via a PerkinElmer SPECTRUM 100 FTIR spectrometer. The photoluminescence (PL) spectra were acquired from a JASCO FP-8500 fluorescence spectrophotometer at the excitation wavelength of 300 nm. UV–vis diffuse reflectance spectra (DRS) were measured on a JASCO V-750 UV–vis spectrophotometer. In order to observe the surface morphologies of photocatalysts, scanning electron microscopy (SEM) and transmission electron microscopy (TEM) images were obtained via HITACHI S-4300 and JEOL JEM-1011, respectively. The Brunauer–Emmett–Teller (BET) specific surface areas and the pore size distributions of

photocatalysts were analyzed via the nitrogen adsorption/desorption isotherms from BEL-SORP-miniII. A SHIMADZU UV-2450 UV–visible spectrometer was employed to examine the concentration and/or intensity changes of MO during the photocatalytic reaction.

The photoelectrochemical experiments were carried out on a Princeton Applied Research VersaSTAT 3 electrochemical workstation with a conventional three-electrode cell. The reference electrode and counter electrode were applied to the Ag/AgCl electrode and platinum electrode, respectively. In order to prepare the working electrode, a slurry consisting of a proper quantity of photocatalysts, 5 wt.% Nafion (R) perfluorinated resin solution, and 2-propanol was dropped onto indium tin oxide (ITO) glass, and then the electrode was deposited. The electrolyte was an aqueous solution of 0.2 mol/L aqueous sodium sulfate (Na_2SO_4). The light source for measuring the on/off response was a 100 W xenon lamp equipped with a cut-off filter ($\lambda \geq 420$ nm).

3.4. Photocatalytic Experiments

The photocatalytic activities of the synthesized photocatalysts were evaluated via the dye-degradation of methyl orange (MO) under visible light irradiation at room temperature. An amount of 20 mg of each photocatalyst was dispersed in 35 mL of MO solution (10 mg/L). Before light irradiation, the suspension was magnetically stirred in the dark for 30 min to achieve adsorption/desorption equilibrium of MO with photocatalysts. The photoreaction system was exposed to a 500 W xenon lamp equipped with a cut-off filter ($\lambda \geq 420$ nm) as a visible light source. At regulated intervals of time, a fixed volume of the reaction mixture was collected and centrifuged to remove the catalyst particulates. The supernatant solution was then analyzed via a UV–visible spectrophotometer ($\lambda = 460$ nm).

4. Conclusions

In the present study, a novel visible-light-driven photocatalyst labeled W-Sn_3O_4@CTAB was prepared by modifying tungsten into mixed-valence tin oxides (Sn_3O_4), using the solvothermal method with CTAB as a structure-directing agent. The characterization of the crystallographic phase properties and chemical structure reveals that tungsten was successfully introduced into Sn_3O_4 materials for the first time and that CTAB controlled the final photocatalyst morphology well. Consequently, tungsten modification and the CTAB additive have a strong effect on visible light response capability and photocatalytic performance due to the formation of tungsten-derived impurity levels within and optimization of the band gap structure of Sn_3O_4. The photocatalytic performance of W-Sn_3O_4@CTAB (0.03 g) was evaluated via the dye-decolorization efficiency of MO, indicating that W-Sn_3O_4@CTAB most efficiently achieved almost complete decolorization within 40 min under visible light irradiation. The enhanced photocatalytic activity of the proposal materials is attributed to the increased light absorption and the decreased recombination of photogenerated electron–hole pairs. This research demonstrates unique approaches to developing tin oxide-based materials and their potential to enhance photocatalytic activity for pollutant removal.

References

1. Lin, Y.; Yang, C.; Wu, S.; Li, X.; Chen, Y.; Yang, Y.C. Construction of built-in electric field within silver phosphate photocatalyst for enhanced removal of recalcitrant organic pollutants. *Adv. Funct. Mater.* **2020**, *30*, 2002918. [CrossRef]
2. Anjaneya, O.; Shrishailnath, S.S.; Guruprasad, K.; Anand, S.N.l.; Mashetty, S.B.l.; Karegoudar, T.B. Decolourization of Amaranth dye by bacterial biofilm in batch and continuous packed bed bioreactor. *Int. Biodeterior. Biodegrad.* **2013**, *79*, 64–72. [CrossRef]
3. Sun, L.; Mo, Y.; Zhang, L. A mini review on bio-electrochemical systems for the treatment of azo dye wastewater: State-of-the-art and future prospects. *Chemosphere* **2022**, *294*, 133801. [CrossRef]
4. Zhang, J.; Yuan, X.; Jiang, L.; Wu, Z.; Chen, X.; Wang, H.; Zeng, G. Highly efficient photocatalysis toward tetracycline of nitrogen doped carbon quantum dots sensitized bismuth tungstate based on interfacial charge transfer. *J. Colloid Interface Sci.* **2018**, *622*, 296–306. [CrossRef] [PubMed]
5. Li, J.; Dong, X.; Zhang, G.; Cui, W.; Cen, W.; Wu, G.; Lee, S.C.; Dong, F. Probing ring-opening pathways for efficient photocatalytic toluene decomposition. *J. Mater. Chem.* **2019**, *7*, 3366–3374. [CrossRef]
6. Abdul, H.; Jina-Ming, P.; Afzal, S.; Hazrat, H.; Wei-dong, H. A systematic review on new advancement and assessment of emerging polymeric cryogels for environmental sustainability and energy production. *Sep. Purif. Technol.* **2023**, *316*, 123678. [CrossRef]
7. Abdul, H.; Anum, S.; Sheng-Qi, C.; Mudasir, N. A comprehensive review on adsorption, photocatalytic and chemical degradation of dyes and nitro-compounds over different kinds of porous and composite materials. *Molecules* **2023**, *28*, 1081. [CrossRef]
8. Pirhashemi, M.; Habibi, Y.A.; Pouranb, S.R. Review on the criteria anticipated for the fabrication of highly efficient ZnO-based visible-light-driven photocatalysts. *J. Ind. Eng. Chem.* **2018**, *62*, 1–25. [CrossRef]
9. Owlad, M.; Aroua, M.K.; Daud, W.A.; Baroutian, S. Removal of hexavalent chromium-contaminated water and wastewater: A review. *Water Air Soil Poll.* **2009**, *200*, 59–77. [CrossRef]
10. Yue, X.; Li, J.; Zhang, T.; Qiu, F.; Yang, D.; Xue, M. In situ one-step fabrication of durable superhydrophobic-superoleophilic cellulose/LDH membrane with hierarchical structure for efficiency oil/water separation. *Chem. Eng. J.* **2017**, *328*, 117–123. [CrossRef]
11. Prasad, A.S.A.; Kumar, G.; Thomas, D.M. Microbial decolorization of azo dys-A mini review. *Bull. Chem. Pharma Res.* **2017**, *1*, 30–39. [CrossRef]
12. Yang, Y.; Wu, Q.; Guo, Y.; Hu, C.; Wang, E. Efficient degradation of dye pollutants on nanoporous polyoxotungstate–anatase composite under visible-light irradiation. *J. Mol. Catal. A Chem.* **2005**, *225*, 203. [CrossRef]
13. Ge, L. Novel Pd/BiVO$_4$ composite photocatalysts for efficient degradation of methyl orange under visible light irradiation. *Mater. Chem. Phys.* **2008**, *107*, 465–470. [CrossRef]
14. Attar, A.S. Binary Zn-doped SnO$_2$/Al$_2$O$_3$ nanotube composites for visible-light-driven photocatalytic degradation of basic blue 41. *ACS Appl. Nano Mater.* **2020**, *3*, 9931–9942. [CrossRef]
15. Mei, L.; Wu, W.; Yang, S.; Xing, X.Z.; Ren, F.; Xiao, X.; Jiang, C. Design of enhanced catalysts by coupling of noble metals (Au,Ag) with semiconductor SnO$_2$ for catalytic reduction of 4-nitrophenol. *Part. Part. Syst. Char.* **2016**, *33*, 212–220. [CrossRef]
16. Prakash, K.; Senthil Kumar, P.; Pandiaraj, S.; Saravanakumar, K.; Karuthapandian, S. Controllable synthesis of SnO$_2$ photocatalyst with superior photocatalytic activity for the degradation of methylene blue dye solution. *J. Exp. Nanosci.* **2016**, *11*, 1138–1155. [CrossRef]
17. Seko, A.; Togo, A.; Oba, F.; Tanaka, I. Structure and stability of a homologous series of tin oxides. *Phys. Rev. Lett.* **2008**, *100*, 045702. [CrossRef] [PubMed]
18. Berengue, O.M.; Simon, R.A.; Chiquito, A.J.; Dalmaschio, C.J.; Leite, E.R.; Guerreiro, H.A.; Guimarñaes, F.E.G. Semiconducting Sn$_3$O$_4$ nanobelts: Growth and electronic structure. *J. Appl. Phys.* **2010**, *107*, 033717. [CrossRef]
19. Mone, P.; Mardikar, S.P.; Balgude, S. Morphology-controlled synthesis of Sn$_3$O$_4$ nanowires for enhanced solar-light driven photocatalytic H$_2$ production. *Nano-Struct. Nano-Objects* **2020**, *24*, 100615. [CrossRef]
20. Sun, M.; Yan, T.; Qu, T.; He, Y.; Shao, Y.; Wei, D.; Du, B. Self-assembled hierarchical Sn$_3$O$_4$-multi-wall carbon nanotubes: Facile fabrication, promoted charge separation, and enhanced photocatalytic performances. *Mater. Res. Bull.* **2018**, *103*, 104–113. [CrossRef]
21. Jaramillo-Páez, C.; Navío, J.A.; Hidalgo, M.C.; Macías, M. High UV-photocatalytic activity of ZnO and Ag/ZnO synthesized by a facile method. *Catal. Today* **2017**, *284*, 121–128. [CrossRef]
22. Han, Y.; Wi, M.; Qu, S.; Zhong, M. Ag@AgCl quantum dots embedded on Sn$_3$O$_4$ nanosheets towards synergistic 3D flower-like heterostructured microspheres for efficient visible-light photocatalysis. *Ceram. Int.* **2020**, *46*, 24060–24070. [CrossRef]
23. Ki, S.J.; Park, Y.K.; Kim, J.S.; Lee, W.J.; Lee, H.; Jung, S.C. Facile preparation of tungsten oxide doped TiO$_2$ photocatalysts using liquid phase plasma process for enhanced degradation of diethyl phthalate. *Chem. Eng. J.* **2019**, *377*, 120087. [CrossRef]
24. Ma, J.S.; Lin, L.Y.; Chen, Y.S. Facile solid-state synthesis for producing molybdenum and tungsten co-doped monoclinic BiVO$_4$ as the photocatalyst for photoelectrochemical water oxidation. *Int. J. Hydrog. Energy* **2019**, *44*, 7905–7914. [CrossRef]
25. Liu, X.; Liang, B.; Yang, J.; Li, Q. Solvent effect on morphological evolution and photocatalytic property of α-SnWO$_4$. *J. Taiwan Inst. Chem. Eng.* **2019**, *95*, 575–582. [CrossRef]
26. Wang, Q.L.; Li, H.B.; Jiang, H.Y.; Ding, S.T.; Song, Z.W.; Shi, J.S. Effect of solvent on α-SnWO$_4$ photocatalyst for degradation of methyl orange under visible light irradiation. *Mater. Technol.* **2015**, *30*, 288–293. [CrossRef]

27. Chankhanittha, T.; Watcharakitti, J.; Nanan, S. PVP-assisted synthesis of rod-like ZnO photocatalyst for photodegradation of reactive red (RR141) and Congo red (CR) azo dyes. *J. Mater. Sci. Mater. Electron.* **2019**, *30*, 17804–17819. [CrossRef]

28. Sánchez-Martínez, D.; Gomez-Solis, C.; Torrs-Martinez, M. CTAB-assisted ultrasonic synthesis, characterization and photocatalytic properties of WO₃. *Mater. Res. Bull.* **2015**, *61*, 165–172. [CrossRef]

29. Rajeev, Y.N.; Magdalane, C.M.; Ramalingam, G.; Kumar, L.B.; Alwadai, N.; Al-Buriahi, M.S. Photocatalytic activity of hierarchical CTAB-assisted TiO₂ nanoparticles for polluted water treatment using solar light illumination. *Appl. Phys. A* **2022**, *128*, 299. [CrossRef]

30. Stefan, M.; Lostean, C.; Pana, O.; Popa, A.; Toloman, D.; Macavei, S.; Perhaita, I.; Barbu-Tudoran, L.; Silipas, D. Interface tailoring of SnO₂–TiO₂ photocatalysts modified with anionic/cationic surfactants. *J. Mater. Sci.* **2020**, *55*, 3279–3298. [CrossRef]

31. Shen, A.; Zhao, L.; Guo, L. Crystallite, optical and photocatalytic properties of visible-light-driven ZnIn2S4 photocatalysts synthesized via a surfactant-assisted hydrothermal method. *Mater. Res. Bull.* **2009**, *44*, 100–105. [CrossRef]

32. Sun, W.; Zhang, S.; Liu, Z.; Wang, C.; Mao, Z. Studies on the enhanced photocatalytic hydrogen evolution over Pt/PEG-modified TiO2 photocatalysts. *Int. J. Hydrog. Energy* **2023**, *33*, 1112–1117. [CrossRef]

33. Balgude, S.D.; Sethi, Y.A.; Kale, B.B.; Munirathnam, N.R.; Amalnerkar, D.P.; Adhyapak, P.V. Nanostructured layered Sn₃O₄ for hydrogen production and dye degradation under sunlight. *RSC Adv.* **2016**, *6*, 95663–95669. [CrossRef]

34. Balgude, S.D.; Sethi, Y.A.; Kale, B.B.; Amalnerkar, D.P.; Adhyapak, P.V. ZnO decorated Sn₃O₄ nanosheet nano-heterostructure: A stable photocatalyst for water splitting and dye degradation under natural sunlight. *RSC Adv.* **2019**, *9*, 10289–10296. [CrossRef] [PubMed]

35. Rajeshwaran, P.; Sivarajan, A.; Raja, G.; Madhan, D.; Rajkumar, P. Effect of tungsten (W⁶⁺) metal ion dopant on structural, optical and photocatalytic activity of SnO₂ nanoparticles by a novel microwave method. *J. Mater. Sci.-Mater. Electron.* **2016**, *27*, 2419–2425. [CrossRef]

36. Chen, X.; Wu, Z.; Gao, Z.; Ye, B.C. Effect of different activated carbon as carrier on the photocatalytic activity of Ag-N-ZnO photocatalyst for methyl orange degradation under visible light irradiation. *Nanomaterials* **2017**, *7*, 258. [CrossRef]

37. Ai, F.; Zhao, G.; Lv, W.; Lin, J. Facile synthesis of cetyltrimethylammonium bromide-loaded mesoporous silica nanoparticles for efficient inhibition of hepatocellular carcinoma cell proliferation. *Mater. Res. Express* **2020**, *7*, 085008. [CrossRef]

38. Yang, L.Q.; Lv, M.F.; Song, Y.; Yin, K.Y.; Wang, X.L.; Cheng, X.L.; Cao, K.S.; Li, S.T.; Wang, C.; Yao, Y.F.; et al. Porous Sn₃O₄ nanosheets on PPy hollow rod with photo-induced electrons oriented migration for enhanced visible-light hydrogen production. *Appl. Catal. B* **2020**, *279*, 119341. [CrossRef]

39. Fukumoto, M.; Hirose, Y.; Benjamin, W.; Nakao, S.; Kimura, K.; Hayashi, K.; Sugisawa, Y.; Sekiba, D.; Scanlon, D.; Hasegawa, T. Ligand field-induced exotic dopant for infrared transparent electrode: W in rutile SnO₂. *Adv. Funct. Mater.* **2022**, *32*, 210832. [CrossRef]

40. Uemura, Y.; Kido, D.; Wakisaka, Y.; Uehara, H.; Ohba, T.; Niwa, Y.; Nozawa, S.; Sato, T.; Ichiyanagi, K.; Fukaya, R.l.; et al. Dynamics of photoelectrons and structural changes of tungsten trioxide observed by femtosecond transient XAFS. *Angew. Chem. Int. Ed.* **2016**, *55*, 1364–1367. [CrossRef]

41. Chen, Y.N.; Zhu, G.Q.; Hojamberdiev, M.; Gao, J.Z.; Zhu, R.L.; Wang, C.H.; Wei, X.M.; Liu, P. Three-dimensional Ag₂O/Bi₅O₇I p–n heterojunction photocatalyst harnessing UV–vis–NIR broad spectrum for photodegradation of organic pollutants. *J. Hazard. Mater.* **2018**, *344*, 42–54. [CrossRef]

42. Cho, I.S.; Kwak, C.H.; Kim, D.W.; Lee, S.; Hong, K.S. Photophysical, Photoelectrochemical, and Photocatalytic Properties of novel SnWO₄ oxide semiconductors with narrow band gaps. *J. Phys. Chem. C* **2009**, *113*, 10647–10653. [CrossRef]

43. Manikandan, M.; Tanabe, T.; Li, P.; Ueda, S.; Ramesh, G.V.; Kodiyath, R.; Wang, J.; Hara, T.; Dakshanamoorthy, A.; Ishihara, S.; et al. Photocatalytic water splitting under visible light by mixed-valence Sn₃O₄. *ACS Appl. Mater. Interfaces* **2016**, *6*, 3790. [CrossRef]

44. Wang, D.; Lin, Z.l.; Miao, C.; Jiang, W.; Li, H.; Liu, C.; Che, G. An S-scheme photocatalyst constructed by modifying Ni-doped Sn₃O₄ micro-flowers on g-C3N4 nanosheets for enhanced visible-light-driven hydrogen evolution. *J. Ind. Eng. Chem.* **2022**, *113*, 380–388. [CrossRef]

45. Yu, H.; Shi, R.; Zhao, Y.; Bian, T.; Zhao, Y.; Zhou, C.; Waterhouse, G.I.N.; Wu, L.Z.; Tung, C.H.; Zhang, T. Alkali-assisted synthesis of Nitrogen Deficient Graphitic Carbon Nitride with Tunable Band Structures for Efficient Visible-Light-Driven Hydrogen Evolution. *Adv. Mater.* **2017**, *29*, 1605148. [CrossRef] [PubMed]

46. Huda, A.; Suman, P.H.; Torquato, L.D.M.; Silva, B.F.; Handoko, C.T.; Gulo, F.; Zanoni, M.V.B.; Orlandi, M.O. Visible light-driven photoelectrocatalytic degradation of acid yellow 17 using Sn₃O₄ flower-like thin films supported on Ti substrate (Sn₃O₄/ TiO₂/Ti). *J. Photochem. Photobiol. A* **2019**, *376*, 196–205. [CrossRef]

47. Hong, Y.; Zengwei, L.; Weifeng, L. Single-source-precursor-assisted synthesis of porous WO₃/g-C₃N₄ with enhanced photocatalytic property. *Colloids Surf. A* **2019**, *582*, 123857. [CrossRef]

48. Qinglan, C.; Shiyun, L.; Yongqiang, W.; Shaomin, Z. Red blood cell-like hollow TiO₂@WO₃ microspheres as highly efficient photocatalysts for degradation of organic pollutants. *Inorg. Chem. Commun.* **2023**, *148*, 110307. [CrossRef]

49. Feng, Q.; Yaya, M.; Shizheng, Z.; Changyuan, H.; Lin, W.; Ruofan, Y.; Yanting, M.; Cuiqing, Z. Construction of novel Z-scheme N-CQDs/Sn₃O₄ heterojunction for excellent photocatalytic degradation of organic pollutant. *J. Clust. Sci.* **2022**, *33*, 913. [CrossRef]

50. Ruiqi, Y.; Yanchen, J.; Longwei, W.; Guoxin, S.; Aizhu, W.; Longhua, D.; Na, R.; Yawei, L.; Jian, Z.; Xin, Y. Crystalline Ni-doped Sn₃O₄ nanosheets for photocatalytic H₂ production. *ACS Appl. Nano Mater.* **2020**, *3*, 9268–9275. [CrossRef]

51. Zhang, L.; Xinyu, L.; Xing, Z.; Wei, Z.; Jinwen, M.; Qiushi, W.; Shi, S. Sulfur-doped Sn_3O_4 nanosheets for improved photocatalytic performance. *J. Alloys Compd.* **2023**, *961*, 170904. [CrossRef]

52. Saison, T.; Gras, P.; Chemin, N.; Chanéac, C.; Durupthy, O.; Brezová, V.; Colbeau-Justin, C.; Jolivet, J.P. New insights into Bi_2WO_6 properties as a visible-light photocatalyst. *J. Phys. Chem. C* **2013**, *117*, 22656–22666. [CrossRef]

53. Naik, B.; Manoratne, C.H.; Chandrashekhar, A.; Iyer, A.; Prasad, V.S.; Ghosh, N.N. Preparation of TiO_2, Ag-doped TiO_2 nanoparticle and TiO_2–SBA-15 nanocomposites using simple aqueous solution-based chemical method and study of their photocatalytical activity. *J. Exp. Nanosci.* **2013**, *8*, 462–479. [CrossRef]

54. Li, G.T.; Wong, K.H.; Zhang, X.W.; Hu, C.; Yu, J.C.; Chan, R.C.Y.; Wong, P.K. Degradation of Acid Orange 7 using magnetic AgBr under visible light: The roles of oxidizing species. *Chemosphere* **2009**, *76*, 1185–1191. [CrossRef] [PubMed]